Visualization of orbital twig edge states in phononic graphene lattices

Feng Gao,[1] Yu-Gui Peng,[1,*] Xiao Xiang,[1] Qi-Li Sun,[1] Chen Zheng,[1] Bin Li,[2] and Xue-Feng Zhu[1,†]

[1] *School of Physics and Innovation Institute, Huazhong University of Science and Technology, Wuhan 430074, China*

[2] *School of Mechanical Engineering, Wuhan Polytechnic University, Wuhan 430023, China*

(Received 26 October 2023; revised 2 February 2024; accepted 15 March 2024; published 2 April 2024)

Edge-dependent states in electronic and synthetic graphenes have stimulated extensive research interests in recent years. The orbital degree of freedom (ODOF), facilitating the understanding of exotic phenomena in condensed matter, supplies a powerful base to explore boundary topological properties, which has not yet been investigated extensively in classical-wave realms such as acoustic systems. Here, we experimentally demonstrate orbital-dependent acoustic twig edge states in multi-ODOF systems as degenerate-orthogonal p orbitals are introduced. We analyze and discuss the band structures of orbital strip supercell lattices with the twig and zigzag edges by using the tight-binding method (TBM) and full-wave simulation (FWS). We visualize fourfold zero-energy orbital twig edge states that form the complete flat band across the Brillouin zone, characterized by nontrivial topological windings. Moreover, we unravel the selective excitation of the orbital twig edge states in experiments. Our findings advance the field for understanding the interplay between graphene edge states and acoustic orbitals as well as broaden the potential application opportunities of Dirac materials such as trapping and sensing.

DOI: 10.1103/PhysRevApplied.21.044005

I. INTRODUCTION

Graphene, a two-dimensional (2D) honeycomb lattice (HCL) of carbon atoms, has inspired many fascinating studies in the past few decades [1]. The edge-dependent electronic states of graphene strip supercells [2,3] and their applications in spintronic devices [4,5] have been extensively investigated. Analogous to electronic graphene, various artificial graphene lattices have been proposed in different fields, which overcome the limitations of real materials. One of the most remarkable successes for the synthetic graphenelike lattices lies in the explorations and demonstrations of topological insulators in different systems, such as elastics [6–10], photonics [11–17], and acoustics [18–25]. In acoustics, for example, strategies for one-way robust edge propagation of sound were proposed by using circularly flowing air and angular-momentum-biased graphenelike resonator lattices [18,19]. The acoustic spin Hall effect was experimentally realized by artificial phononic graphene [20]. By considering time-modulated graphenelike acoustic lattices, Floquet topological insulators for sound were demonstrated [21]. Moreover, acoustic valley Hall topological insulators were demonstrated in HCLs [23].

Originating from the condensed-matter physics, the ODOFs have attracted extensive attention and been extended to the intriguing topology investigations of the classical-wave systems. For example, in photonics, quadrupolar topological insulators were realized with synthetic flux induced by s-orbital and p-orbital modes [26] and topological bound states with orbital angular momentum [27]. In phononics, apart from the acoustic quantum spin Hall effect realized by the orbital clusters [20], some interesting orbital-related acoustic topological effects or phases have been realized with p orbitals [28–31], such as Montage operation [28], one-dimensional (1D) counterintuitive orbital topological edge states [29], orbital Möbius, and higher-order topological insulators [30,31].

Hitherto three classical types of edges, including the zigzag, bearded, and armchair edges, have been discussed in graphene [32]. The zigzag and bearded edges have twofold edge states located in different regions that are complementary to each other in the 1D Brillouin zone, giving rise to an "assembly" flat band, while the flawless armchair edge has no edge modes [18,19]. The existing analyses have shown that the three different types of edge states can be topologically defined by the winding characteristics of the Bloch Hamiltonian [33,34]. Moreover, other geometrical edges, such as the decorated armchair edges with Klein nodes, have also been presented via edge modifications [35,36]. Very recently, another type of edge in graphene, called the twig edge, was demonstrated in the photonic platform [37].

Previous explorations on topological edge modes of graphene lattices mainly focus on the single-ODOF

*ygpeng@hust.edu.cn
†xfzhu@hust.edu.cn

scenarios, which has not yet been studied in the acoustic multi-ODOF systems.

In this work, we focus on the paired degenerate p orbitals in each acoustic cavity and demonstrate versatile orbital-dependent twig edge states in the acoustic HCL via TBM, FWS, and experiments. By employing strip supercells of the orbital HCLs, we discuss the band structures and topological properties of the twig and zigzag edges. We illustrate degenerate zero-energy fourfold orbital twig edge states characterized by different windings. In experiments, we demonstrate the orbital-dependent twig edge states with selective excitation property with three-dimensional (3D) printed sample. Our findings expand the single ODOF to multiple ODOF domains for acoustic graphene edge states, showing a promising prospective on the orbital-dependent applications such as trapping and sensing.

II. ACOUSTIC HCL WITH SINGLE ODOF

We start from discussing the features of the twig edge in the HCL and its construction in acoustic single-ODOF system. Figure 1(a) shows a finite experimental sample with twig and zigzag boundaries, which was fabricated by 3D-printing technique. The cavity-tube strategy, where the hoppings are easy to tune, is employed for constructing the acoustic HCL model. Physically, the site resonators emulate atomic orbitals and the connecting tubes introduce hoppings between them in the acoustic HCL. Each resonator is an air-filled cylindrical cavity with hard walls, for which the height and diameter are $h = 30$ mm and $d_1 = 20$ mm, respectively. The diameters of linking waveguides, relating to the hopping strengths t_1, t_2, and t_3, are $d_2 = 6$ mm, and the lengths of the waveguides locating at $h/4(3h/4)$ are $l = 13$ mm. By tuning the diameter d_2, length l, and positions of the connecting waveguides, the coupling strength can be tailored on demand. Resting with the TBM and the basic vectors $\mathbf{a}_1 = \left(\sqrt{3}a/2, -a/2\right)$, $\mathbf{a}_2 = (0, -a)$ originating from the primitive cell as marked in Fig. 1(a), we can derive the Bloch Hamiltonian

$$H(\mathbf{k}) = -\begin{pmatrix} 0 & D(\mathbf{k}) \\ D^{\dagger}(\mathbf{k}) & 0 \end{pmatrix},$$
$$D(\mathbf{k}) = t_1 e^{i\mathbf{k}\mathbf{a_1}} + t_2 + t_3 e^{i\mathbf{k}\mathbf{a_2}} \quad (1)$$

where t_2 (t_1, t_3) means the intracell (intercell) couplings, and a is the lattice constant. Notably, each unit-cell as well as the Bloch Hamiltonian features two different boundary conditions along x and y axes.

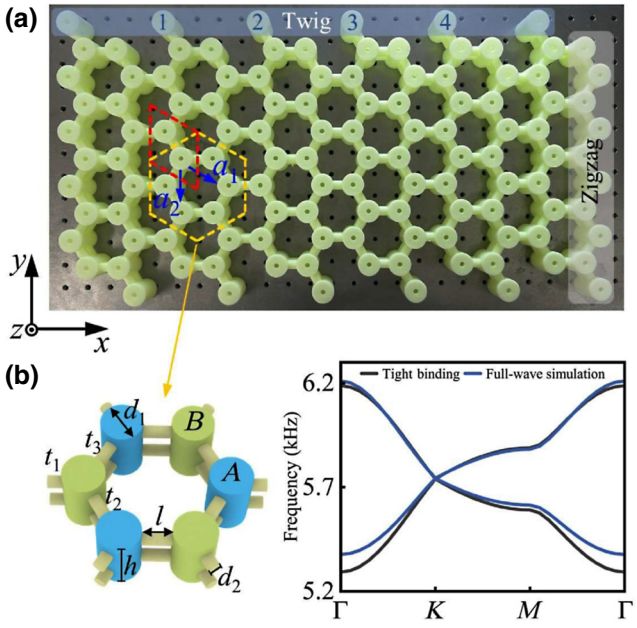

FIG. 1. Acoustic HCL with different edges. (a) A sample with twig (dark-shaded region) and zigzag (light-shaded region) edges. The unit-cell is marked by the dashed red rhombus. The basic vectors $\mathbf{a}_1$ and $\mathbf{a}_2$ are $\mathbf{a}_1 = \left(\sqrt{3}a/2, -a/2\right)$ and $\mathbf{a}_2 = (0, -a)$, where a is the lattice constant. t_1, t_2, and t_3 represent the nearest couplings between **A** and **B** sublattice. The inset denotes an acoustic HCL with two sublattices (**A**, **B**), which is constructed by cylindrical resonator and linking tubes. d_1 (d_2) and h (l) represent the diameters and height (length) of the resonator (tube), respectively. The tubes are located at $h/4$ and $3h/4$ in the dimer unit, respectively. (b) The bulk bands for the acoustic HCL obtained by TBM (black lines) and the bands derived by FWS (blue lines), which are in good agreements.

III. ANALYSES FOR ACOUSTIC TWIG AND ZIGZAG EDGE STATES

Next, we use a strip supercell with periodical boundary conditions along the x direction and open boundary conditions along the y direction to investigate the unique properties of the twig edge based on TBM and FWS. Figure 2(a) shows the projected energy bands of one supercell by TBM. The red lines represent the twofold degenerate twig edge states that span the entire Brillouin zone, forming a 1D dispersionless flat band. Note that this complete band observed at the twig edge is different from the combined one comprising the edge states from different types (zigzag and bearded) of HCL edges. Then, we construct the strip supercell model based on the HCL cavity-tube unit in Fig. 1(a), and the simulated projected band structures by FWS are shown in Fig. 2(b), which agree well with those in Fig. 2(a). For the zigzag edge, the supercell is periodical in the y direction and finite in the x direction. The bands generated by the TBM and FWS are shown in Figs.

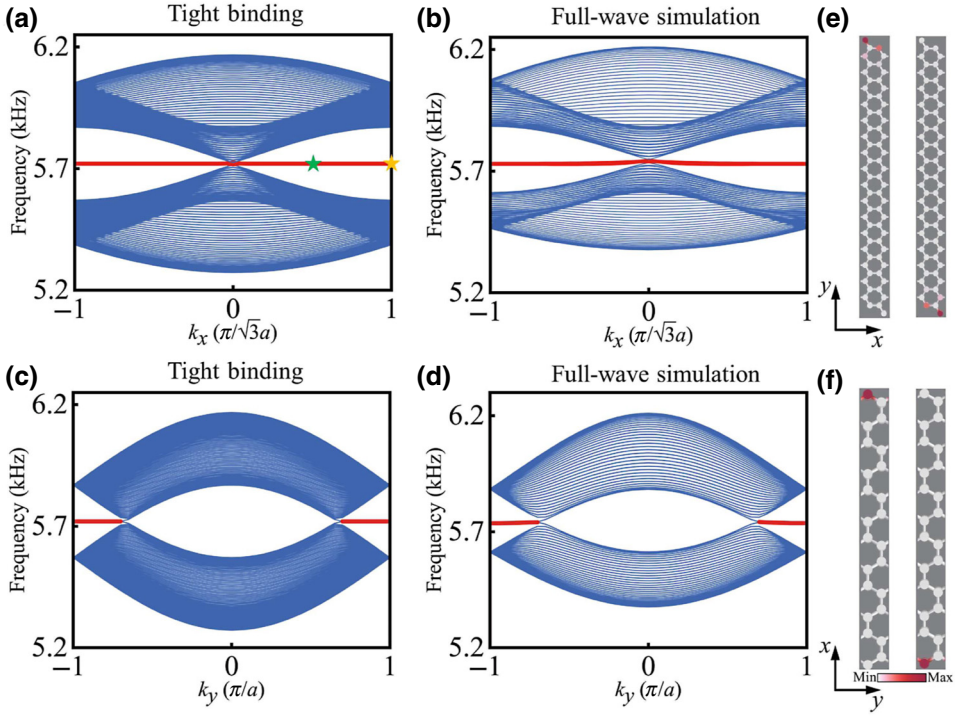

FIG. 2. The topological features of acoustic twig and zigzag edge states. (a),(b) The projected energy bands for a ribbon supercell with twig edges acquired by the TBM and FWS under periodical boundary condition along the x direction and open boundary condition along the y direction. A pair of twofold edge bands marked by the red line represent the twig edge states across the whole Brillouin zone, forming a complete flat band. The green (orange) stars indicate the modes at $k_x = \pi/2\sqrt{3}a$ $\left(k_x = \pi/\sqrt{3}a\right)$. (c),(d) The projected energy bands for a ribbon supercell with zigzag edges acquired by the TBM and FWS under periodical boundary condition along the y direction and open boundary condition along the x direction. The existing zigzag edge states are denoted by the red line. (e),(f) The simulated eigenfields for twig and zigzag edge states, respectively.

2(c) and 2(d), respectively, which agree well with each other. The zigzag edge states are complementary to that of the bearded edge states and the transition point locates at $k_y = 2\pi/3a$ ($k_y = -2\pi/3a$). To show the twig and zigzag edges intuitively, the intensity field distributions of their supercells are presented in Figs. 2(e) and 2(f).

IV. EXPERIMENTAL DEMONSTRATION OF ACOUSTIC TWIG EDGE STATES

We conduct several acoustic experiments to characterize the twig edge states and the associated distinct features by using the sample in Fig. 1(a). To well excite the acoustic twig edge states, we consider a proper sound source with specific phases matching those of the theoretically predicted or numerically simulated edge states in Figs. 2(a) and 2(b). For example, for the eigenmode at $k_x = \pi/\sqrt{3}a$, as marked by the orange star in Fig. 2(a), a phase factor of $\exp(i\pi)$ exists between the nearest-neighboring supercells. In experiments, four sound sources with the phase difference of $\Delta\phi = \pi$ between the nearest-neighboring supercells were inserted in the cavities numbered 1, 2, 3, 4 in Fig. 1(a) to well excite the twig edge states. The measured amplitude response spectra in the sites 1–4, viz., Probe_1, Probe_2, Probe_3 and Probe_4, are shown in Fig. 3(a), respectively. Obviously, four outstanding peaks emerge in the spectra, corresponding to the frequency of the twig edge mode at 5904 Hz. Besides, the corresponding intensity field distribution was measured and shown in Fig. 3(b). Clearly, for the twig edge on top of the sample, the detected acoustic energy was majorly localized at the edge and distributed only at sites **B**, which form the edge states in agreement with the modes in Fig. 2(a). Here to decrease the finite-size effects along the x direction, the two boundary sites are not excited. Moreover, to elucidate the twig edge modes emerging in a large momentum range, the sound signal with a different transverse momentum is selected, matching the green-star excitation at $k_x = \pi/2\sqrt{3}a$ in Fig. 2(a), and a phase factor of $\exp(i\pi/2)$ between the nearest supercells is considered. By exchanging the phase difference to $\Delta\phi = \pi/2$ for the sources, similar procedures are conducted to excite this

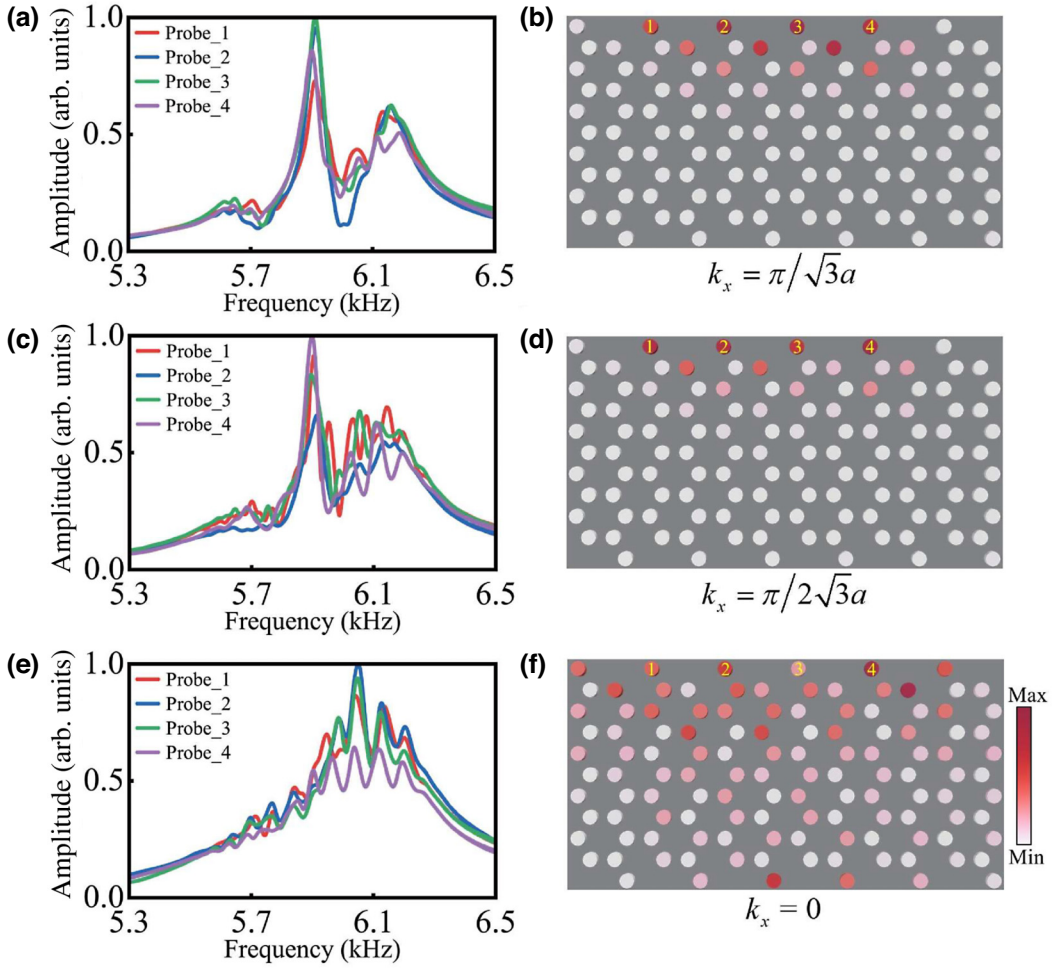

FIG. 3. Experimental verifications for the twig edge states in the acoustic system. (a),(b) The measured pressure amplitude response spectra and the field distribution for the eigenmode at $k_x = \pi/\sqrt{3}a$ as denoted by the orange star in Fig. 2(a). (c),(d) The pressure amplitude response spectra and the field distribution for the eigenmode at $k_x = \pi/2\sqrt{3}a$ as denoted by the green star in Fig. 2(a). (e),(f) The pressure amplitude response spectra and field distribution for the mixed modes at $k_x = 0$.

twig edge state as the one in the case of $k_x = \pi/\sqrt{3}a$, and the detected acoustic response spectra and captured intensity field profiles are, respectively, shown in Figs. 3(c) and 3(d), which also manifest the existence of twig edge states and the related topological characteristics.

In contrast to the zigzag or the bearded edges, which are unable to host edge modes at these two relative spectral positions simultaneously, this is a distinct feature of the twig edge. Additionally, the acoustic response spectra and the associated intensity field profiles for the mixed modes at $k_x = 0$ are also obtained as shown in Figs. 3(e) and 3(f). As we expect, there exists no prominent peak in the spectrum of Fig. 3(e) at the frequency as the cases in Figs. 3(a) and 3(c), and the acoustic wave propagates into the bulk rather than localizing only at the twig edge in Fig. 3(f). The reason is that sound signal for the mixed-mode excitation is not the edge eigenmode of the acoustic graphene but the bulk-mode superposition at $k_x = 0$. Therefore, it cannot transmit steadily along the top boundary resonators, compared with the edge eigenmode excitation.

V. ORBITAL-DEPENDENT ACOUSTIC TWIG EDGE STATES

Next, we investigate the intriguing orbital-dependent twig edge states and related topological properties in a multi-ODOF system. Specially, a pair of degenerate orthogonal p (p_1 and p_2) orbital modes are introduced to construct a multi-ODOF system and the disk-shaped resonator hosting the demanding orbital modes is designed. The corresponding field patterns for the p orbitals in the resonator are shown in the inset of Fig. 4(a). In this work, the height and diameter of disk-shaped resonator correspond to $h_1 = 10$ mm and $d_3 = 36$ mm, respectively. The diameters of connecting waveguides located at $h_1/2$ are

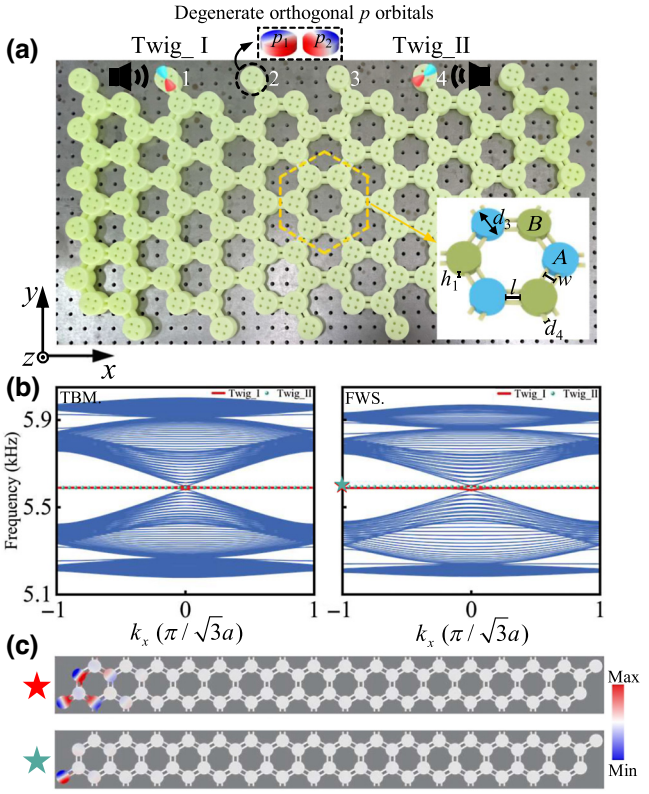

FIG. 4. Zero-energy orbital twig edge states in acoustic HCL with multi-ODOFs. (a) Fabricated sample. The inset on the sample shows field modes for degenerate orthogonal p orbitals (p_1 and p_2) in the disk-shaped resonator. The other inset shows an orbital acoustic HCL with two sublattices (**A**, **B**), which is built by the disk-shaped resonator and paired parallel tubes. d_3 (d_4) represent the diameter of the resonator (tube). h_1 and l are the height of resonator and interval spacing between two adjacent resonators, respectively. w is the interval spacing between the paired tubes located at $h_1/2$. (b) Left: projected energy bands of a ribbon supercell with twig edges obtained by TBM under periodic boundary condition along the x direction and open boundary condition along the y direction in the multi-ODOF acoustic system. Right: projected energy bands of a ribbon supercell obtained by FWS. (c) The pressure fields of zero-energy Twig_I and Twig_II edge states in the supercell as marked by the color-encoded stars in (b).

$d_4 = 5$ mm, and the interval between two adjacent resonators is $l = 13$ mm. The interval between the paired waveguides is $w = d_3/3$.

Based on the TBM and the basic vectors, as marked in Fig. 1(a), the Bloch Hamiltonian in the multi-ODOF system can be obtained as

$$H_1(\mathbf{k}) = -\begin{pmatrix} 0 & D_1(\mathbf{k}) \\ D_1^{\dagger}(\mathbf{k}) & 0 \end{pmatrix}, D_1(\mathbf{k}) = \begin{pmatrix} \xi_1 & \xi_2 \\ \xi_2 & \xi_3 \end{pmatrix}, \tag{2}$$

$$\xi_1 = t_\pi + \left(\frac{3}{4}t_\sigma + \frac{1}{4}t_\pi\right)(e^{i\mathbf{k}\mathbf{a}_1} + e^{i\mathbf{k}\mathbf{a}_2}),$$

$$\xi_2 = \left(-\frac{\sqrt{3}}{4}t_\sigma + \frac{\sqrt{3}}{4}t_\pi\right)e^{i\mathbf{k}\mathbf{a}_1} + \left(\frac{\sqrt{3}}{4}t_\sigma - \frac{\sqrt{3}}{4}t_\pi\right)e^{i\mathbf{k}\mathbf{a}_2}$$

$$\xi_3 = t_\sigma + \left(\frac{1}{4}t_\sigma + \frac{3}{4}t_\pi\right)(e^{i\mathbf{k}\mathbf{a}_1} + e^{i\mathbf{k}\mathbf{a}_2}).$$

There exist two different types of couplings, viz., $\boldsymbol{\sigma}$-type bonding and $\boldsymbol{\pi}$-type bonding in the degenerate p orbitals systems. To be specific, $\boldsymbol{\sigma}$ bonding describes the coupling between meta-atoms with the orbital orientation parallel to the coupling direction, while $\boldsymbol{\pi}$ bonding describes the hopping for the orbital orientation vertical to the bonding direction. t_σ and t_π, respectively, represents the corresponding hopping values for two types of bondings.

By means of the TBM and the FWS, we obtained the corresponding projective bands of the ribbon supercell for the orbital HCL as shown in the left and right of Fig. 4(b), respectively, which match with each other well. Clearly, there exist fourfold degenerate zero-energy orbital twig edge modes forming the multifold flat band, which can be further classified in two categories, viz., paired p_1 orbital twig edge state (Twig_I) denoted by the red lines and p_2 orbital twig edge state (Twig_II) marked by the dark green dots. In Fig. 4(c), we present the simulated eigenfield distributions of Twig_I and Twig_II edge states for the ribbon model at the positions denoted by the color-encoded stars in Fig. 4(b).

VI. NONZERO-ENERGY ORBITAL TWIG EDGE STATES AND VERSATILE ORBITAL ZIGZAG EDGE STATES

In the proposed multiple-ODOF acoustic system, apart from the zero-energy orbital twig edge states, there are also abundant nonzero-energy orbital twig edge states located at different frequency windows. As shown in Fig. 5(a), other two types of nonzero-energy orbital twig edge states featured with different field profiles exist at below and above the zero-energy region, which are termed as Twig_III and Twig_IV denoted by the green and orange lines. To better show these nonzero-energy orbital twig edge states, in Fig. 5(b), we present the field distributions of the ribbon model at the positions denoted by color-coded triangles in Fig. 5(a).

Meanwhile, multiple orbital zigzag edge modes emerge at different frequency windows, viz., the zero-energy and nonzero-energy ones as displayed in Fig. 5(c). Specifically, the zigzag edge in the multi-ODOF system hosts twofold zero-energy orbital edge modes termed as Zigzag_I (red lines), distributed in the complementary region to the one in the single-ODOF system in the 1D Brillouin zone, and also possesses nonzero-energy orbital edge modes termed

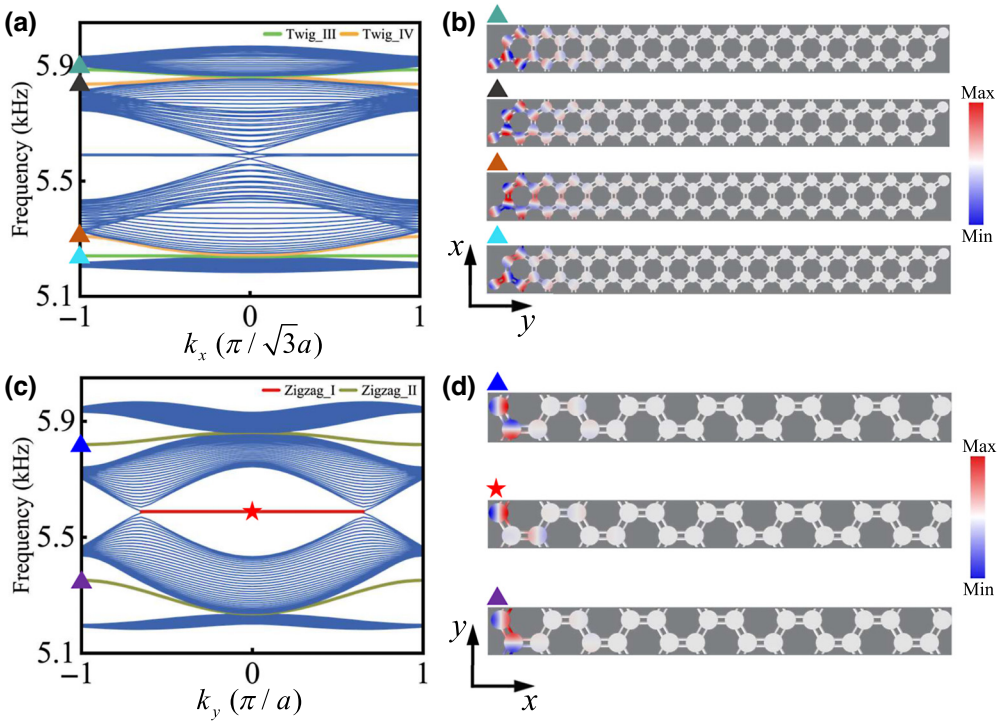

FIG. 5. Nonzero-energy orbital twig edge states and versatile orbital zigzag edge states. (a) Simulated projective energy bands for a ribbon supercell with twig edges in the proposed multi-ODOF acoustic system. The green and orange bands represent different types of nonzero-energy orbital twig edge states, viz., Twig_III and Twig_IV. (b) The pressure fields of orbital twig edge states in the supercell as marked by the color-encoded triangles in (a). (c) Simulated projective energy bands for a ribbon supercell with zigzag edges in the multi-ODOF system. Zero-energy orbital edge states are denoted by the red bands, the distributed region of which is complementary to the one in the single-ODOF system. Dark olivine bands represent for the nonzero-energy orbital zigzag edge states. (d) The pressure fields of orbital zigzag edge states in the supercell as marked by the color-encoded triangles and star in (c).

as Zigzag_II represented by dark olivine bands. Figure 5(d) shows the field profiles of the zigzag-edge ribbon model at the positions marked by color-coded triangles and star in Fig. 5(c).

VII. TOPOLOGICAL INVARIANTS FOR THE MULTI-ODOF SYSTEM

The orbital graphene edge modes are induced by the bulk topologies and can be reflected from the bulk-boundary correspondence [34,38]. The topological invariant can be characterized by the winding number

$$\mathcal{W} = \frac{1}{2\pi}\oint \frac{d}{d\mathbf{k}} \arg[\Delta(\mathbf{k})]d\mathbf{k}, \tag{3}$$

where $\mathbf{k}$ is k_x or k_y resting with the edge direction, and $\Delta(\mathbf{k}) = \xi_1\xi_3 - \xi_2^2$ is the off-diagonal equivalent ingredient of the Hamiltonian in Eq. (2). For the twig and zigzag edges, the Bloch Hamiltonian can be described in the form $H_1(\mathbf{k}) = h(\mathbf{k})\cdot\boldsymbol{\sigma}$, where $h(\mathbf{k}) = \{Re[\Delta(\mathbf{k})], \mathrm{Im}[\Delta(\mathbf{k})]\}$, and the Pauli matrix $\boldsymbol{\sigma}=(\sigma_x,\sigma_y)$.

We use $H_1(\mathbf{k})$ to analyze the topological properties for the orbital twig edge and zigzag edge, the obtained winding loops of which at different k_x and k_y are displayed in Figs. 6(a)–6(f), respectively. Obviously, for the orbital twig edge, the winding numbers remain to be $\mathcal{W}=2$ except $k_x=0$ ($\mathcal{W}=1$), which is indicated by the corresponding windings. This further confirm the fourfold zero-energy orbital twig edge states exist throughout the 1D Brillouin zone, forming the fourfold topological flat band. For the orbital zigzag edge, it can be found the winding number is $\mathcal{W}=1$ at $k_y=0$ but $\mathcal{W}=0$ at $k_y=\pi/a$, and the critical point is $k_y=2\pi/3a$, which is different from the single-ODOF case in Fig. 2. This further confirm the orbital zigzag edge states in the multi-ODOF systems exist in the complementary region to the one in the single-orbital system in the 1D Brillouin zone.

VIII. EXPERIMENTAL DEMONSTRATION FOR THE ORBITAL ACOUSTIC TWIG EDGE STATES

Here, we illustrate the selective excitations of the multiple zero-energy orbital twig edge states in experiments. To form the orbital source, a pair of speakers represented by the dumbbell with phase 0 (red) and π (light blue) are used as sketched on the top sites of the sample in Fig. 4(a). For the excitation of the Twig_I modes at the $k_x=\pi/\sqrt{3}a$, the setting orientation of orbital sources is displayed on the site

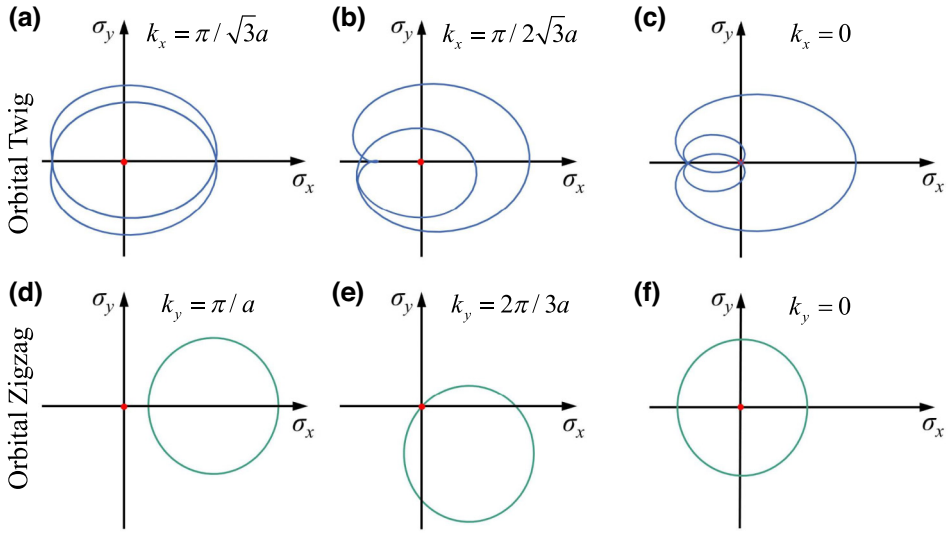

FIG. 6. (a)–(c) Windings for the orbital twig edge modes at different k_x. The red dot denotes the origin point $\mathcal{O}$. (d)–(f) Windings for the orbital zigzag edge modes at different k_y.

resonator numbered 1 in Fig. 4(a), and then the same procedures as those in Fig. 3(a) are conducted. The measured amplitude response spectra in sites 1–4 are, respectively, shown Fig. 7(a), where peaks corresponding to the frequency of the Twig_I edge state emerge in the middle of the spectra. Besides, to illustrate the zero-energy orbital

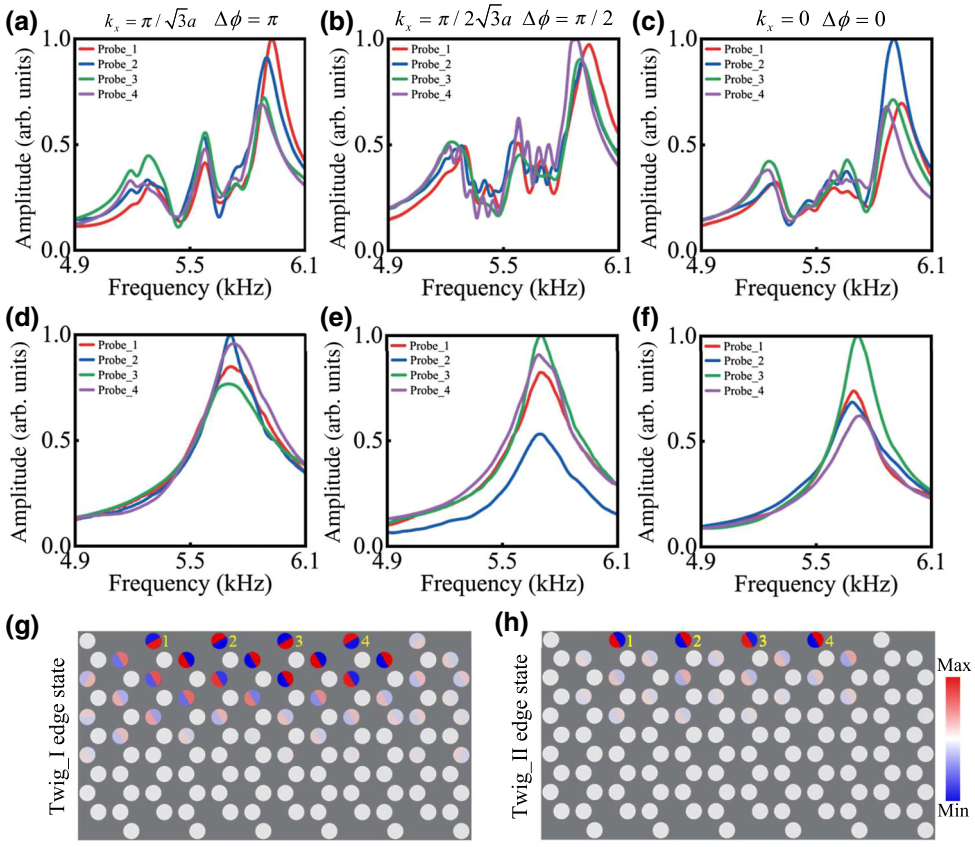

FIG. 7. Experimental demonstration for the orbital-dependent twig edge states. (a)–(c) Detected response spectra for the Twig_I edge modes at $k_x = \pi/\sqrt{3}a$, $k_x = \pi/2\sqrt{3}a$ and $k_x = 0$. (d)–(f) Counterparts for the Twig_II edge modes as those in (a)–(c). (g), (h) Field distributions for the Twig_I and Twig_II edge states with obvious p-orbital features.

twig edge modes existing in a large momentum range, we excited the twig edge at $k_x = \pi/2\sqrt{3}a$ and $k_x = 0$ as four sources with phase difference of $\Delta\phi = \pi/2$ and $\Delta\phi = 0$ between the nearest-neighboring supercells were set, and the detected response spectra are, respectively, shown in Figs. 7(b) and 7(c). It can be found that the Twig_I edge state exists at $k_x = \pi/2\sqrt{3}a$ and is absent at $k_x = 0$. Next, we rotated the sources 90° on the excited resonators as exemplified on the site resonators numbered 4 to well excite the Twig_II edge states at $k_x = \pi/\sqrt{3}a$, $k_x = \pi/2\sqrt{3}a$, and $k_x = 0$. We carried out similar procedures as those in Figs. 7(a)–7(c), and the obtained response spectra are, respectively, displayed in Figs. 7(d)–7(f). As expected, in Figs. 7(d) and 7(e), prominent peaks correspond to the frequency of the Twig_II edge modes emerge in the spectra, but peaks exist in Fig. 7(f) as $k_x = 0$, indicating the preservation of this type of edge state, which is different from the single-ODOF systems. The peak frequency of the Twig_I and Twig_II edge states in the experiments experiences a slight frequency shift due to fabrication imperfections. Moreover, we employed two microphones to detect the frequency and phase responses in each site resonator to capture the field distributions of the Twig_I and Twig_II edge state, which are, respectively, shown in Figs. 7(g) and 7(h). Two types of orbital-dependent twig edge states show obvious p-orbital features. Overall, the interplays between orbitals and graphene edge as well as topological properties can advance the field for the abundant acoustic edge responses and show promising opportunities on the practical applications such as trapping and sensing.

IX. CONCLUSIONS

In summary, a peculiar type of orbital graphene edge state as well as the related properties are theoretically and experimentally demonstrated in the multi-ODOF acoustic systems. By harnessing ribbon supercells, the orbital twig edge states are confirmed to be fourfold degenerate across the Brillouin zone in multi-ODOF scenarios, featuring multifold flat band with orbital characteristics. Moreover, we discuss the multiple zero-energy orbital-dependent twig edge modes and nonzero-energy ones as well as the abundant orbital zigzag edge modes. We further visualize the orbital twig edge states featured with selective excitation in experiments. Our findings open opportunities for the versatile acoustic orbital-related edge states in the Dirac systems and show potentials on orbital-selective functional device applications for trapping and sensing.

ACKNOWLEDGMENTS

This work was supported by Key Research and Development Program of the Ministry of Science and Technology of China under Grant No. 2023YFB4604800 and the National Natural Science Foundation of China through Grant No. 12304492.

[1] A. H. Castro Neto, F. Guinea, N. M. R. Peres, K. S. Novoselov, and A. K. Geim, The electronic properties of graphene, Rev. Mod. Phys. **81**, 109 (2009).
[2] K. Nakada, M. Fujita, G. Dresselhaus, and M. S. Dresselhaus, Edge state in graphene ribbons: Nanometer size effect and edge shape dependence, Phys. Rev. B **54**, 17954 (1996).
[3] L. Brey and H. A. Fertig, Electronic states of graphene nanoribbons studied with the Dirac equation, Phys. Rev. B **73**, 235411 (2006).
[4] Y.-W. Son, M. L. Cohen, and S. G. Louie, Half-metallic graphene nanoribbons, Nature **444**, 347 (2006).
[5] O. V. Yazyev and M. I. Katsnelson, Magnetic correlations at graphene edges: Basis for novel spintronics devices, Phys. Rev. Lett. **100**, 047209 (2008).
[6] P. Wang, L. Lu, and K. Bertoldi, Topological phononic crystals with one-way elastic edge waves, Phys. Rev. Lett. **115**, 104302 (2015).
[7] J. Vila, R. K. Pal, and M. Ruzzene, Observation of topological valley modes in an elastic hexagonal lattice, Phys. Rev. B **96**, 134307 (2017).
[8] S. Li, D. Zhao, H. Niu, X. Zhu, and J. Zang, Observation of elastic topological states in soft materials, Nat. Commun. **9**, 1370 (2018).
[9] Z. Ma, Y. Liu, Y.-X. Xie, and Y.-S. Wang, Tuning of higher-order topological corner states in a honeycomb elastic plate, Phys. Rev. Appl. **19**, 054038 (2023).
[10] H. Fan, B. Xia, L. Tong, S. Zheng, and D. Yu, Elastic higher-order topological insulator with topologically protected corner states, Phys. Rev. Lett. **122**, 204301 (2019).
[11] M. C. Rechtsman, J. M. Zeuner, Y. Plotnik, Y. Lumer, D. Podolsky, F. Dreisow, S. Nolte, M. Segev, and A. Szameit, Photonic Floquet topological insulators, Nature **496**, 196 (2013).
[12] Y. Lumer, Y. Plotnik, M. C. Rechtsman, and M. Segev, Self-localized states in photonic topological insulators, Phys. Rev. Lett. **111**, 243905 (2013).
[13] Y. Plotnik, M. C. Rechtsman, D. Song, M. Heinrich, J. M. Zeuner, S. Nolte, Y. Lumer, N. Malkova, J. Xu, A. Szameit, Z. Chen, and M. Segev, Observation of unconventional edge states in "photonic graphene", Nat. Mater. **13**, 57 (2014).
[14] L. H. Wu and X. Hu, Scheme for achieving a topological photonic crystal by using dielectric material, Phys. Rev. Lett. **114**, 223901 (2015).
[15] M. Milicevic, T. Ozawa, G. Montambaux, I. Carusotto, E. Galopin, A. Lemaitre, L. Le Gratiet, I. Sagnes, J. Bloch, and A. Amo, Orbital edge states in a photonic honeycomb lattice, Phys. Rev. Lett. **118**, 107403 (2017).
[16] M. Milićević, G. Montambaux, T. Ozawa, O. Jamadi, B. Real, I. Sagnes, A. Lemaître, L. Le Gratiet, A. Harouri, J. Bloch, and A. Amo, Type-III and tilted Dirac cones emerging from flat bands in photonic orbital graphene, Phys. Rev. X **9**, 031010 (2019).

[17] T. Biesenthal, L. J. Maczewsky, Z. Yang, M. Kremer, M. Segev, A. Szameit, and M. Heinrich, Fractal photonic topological insulators, Science **376**, 1114 (2022).
[18] X. Ni, C. He, X.-C. Sun, X.-p. Liu, M.-H. Lu, L. Feng, and Y.-F. Chen, Topologically protected one-way edge mode in networks of acoustic resonators with circulating air flow, New J. Phys. **17**, 053016 (2015).
[19] A. B. Khanikaev, R. Fleury, S. H. Mousavi, and A. Alu, Topologically robust sound propagation in an angular-momentum-biased graphene-like resonator lattice, Nat. Commun. **6**, 8260 (2015).
[20] C. He, X. Ni, H. Ge, X.-C. Sun, Y.-B. Chen, M.-H. Lu, X.-P. Liu, and Y.-F. Chen, Acoustic topological insulator and robust one-way sound transport, Nat. Phys. **12**, 1124 (2016).
[21] R. Fleury, A. B. Khanikaev, and A. Alu, Floquet topological insulators for sound, Nat. Commun. **7**, 11744 (2016).
[22] Z. Zhang, Q. Wei, Y. Cheng, T. Zhang, D. Wu, and X. Liu, Topological creation of acoustic pseudospin multipoles in a flow-free symmetry-broken metamaterial lattice, Phys. Rev. Lett. **118**, 084303 (2017).
[23] Z. Zhang, Y. Gu, H. Long, Y. Cheng, X. Liu, and J. Christensen, Subwavelength acoustic valley-Hall topological insulators using soda cans honeycomb lattices, Research **2019**, 5385763 (2019).
[24] L.-Y. Zheng and J. Christensen, Dirac hierarchy in acoustic topological insulators, Phys. Rev. Lett. **127**, 156401 (2021).
[25] H. Xue, Y. Yang, and B. Zhang, Topological acoustics, Nat. Rev. Mater. **7**, 974 (2022).
[26] J. Schulz, J. Noh, W. A. Benalcazar, G. Bahl, and G. von Freymann, Photonic quadrupole topological insulator using orbital-induced synthetic flux, Nat. Commun. **13**, 6597 (2022).
[27] C. Jiang, Y. Wu, M. Qin, and S. Ke, Topological bound modes with orbital angular momentum in optical waveguide arrays, J. Lightwave Technol. **41**, 2205 (2023).
[28] Q.-L. Sun, Y.-G. Peng, F. Gao, B. Li, and X.-F. Zhu, Montage operation of plaquette states in acoustic orbital lattices with type-III Dirac points, Phys. Rev. Appl. **20**, 024025 (2023).
[29] F. Gao, X. Xiang, Y.-G. Peng, X. Ni, Q.-L. Sun, S. Yves, X.-F. Zhu, and A. Alù, Orbital topological edge states and phase transitions in one-dimensional acoustic resonator chains, Nat. Commun. **14**, 8162 (2023).
[30] F. Gao, Y.-G. Peng, Q.-L. Sun, X. Xiang, C. Zheng, and X.-F. Zhu, Topological acoustics with orbital-dependent gauge fields, Phys. Rev. Appl. **20**, 064036 (2023).
[31] F. Gao, Y.-G. Peng, X. Xiang, X. Ni, C. Zheng, S. Yves, X.-F. Zhu, and A. Alù, Acoustic higher-order topological insulators induced by orbital-interactions, Adv. Mater. 2312421 (2024).
[32] M. Kohmoto and Y. Hasegawa, Zero modes and edge states of the honeycomb lattice, Phys. Rev. B **76**, 205402 (2007).
[33] S. Ryu and Y. Hatsugai, Topological origin of zero-energy edge states in particle-hole symmetric systems, Phys. Rev. Lett. **89**, 077002 (2002).
[34] P. Delplace, D. Ullmo, and G. Montambaux, Zak phase and the existence of edge states in graphene, Phys. Rev. B **84**, 195452 (2011).
[35] K. Wakabayashi, S. Okada, R. Tomita, S. Fujimoto, and Y. Natsume, Edge states and flat bands of graphene nanoribbons with edge modification, J. Phys. Soc. Jpn. **79**, 034706 (2010).
[36] W. Jaskólski, A. Ayuela, M. Pelc, H. Santos, and L. Chico, Edge states and flat bands in graphene nanoribbons with arbitrary geometries, Phys. Rev. B **83**, 235424 (2011).
[37] S. Xia, Y. Liang, L. Tang, D. Song, J. Xu, and Z. Chen, Photonic realization of a generic type of graphene edge states exhibiting topological flat band, Phys. Rev. Lett. **131**, 013804 (2023).
[38] R. S. K. Mong and V. Shivamoggi, Edge states and the bulkboundary correspondence in Dirac Hamiltonians, Phys. Rev. B **83**, 125109 (2011).